

Highly Efficient Anisotropic Chiral Plasmonic Metamaterials for Polarization Conversion and Detection

Jing Bai and Yu Yao*



Cite This: *ACS Nano* 2021, 15, 14263–14274



Read Online

ACCESS |



Metrics & More



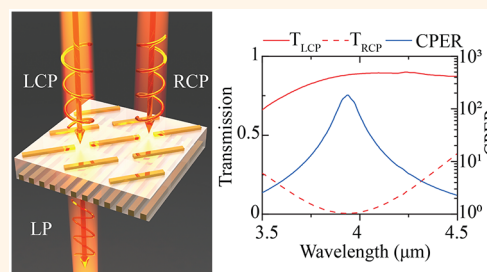
Article Recommendations



Supporting Information

ABSTRACT: Plasmonic chiral metamaterials have attracted broad research interest because of their potential applications in optical communication, biomedical diagnosis, polarization imaging, and circular dichroism spectroscopy. However, optical losses in plasmonic structures severely limit practical applications. Here, we present the design concept and experimental demonstration for highly efficient subwavelength-thick plasmonic chiral metamaterials with strong chirality. The proposed designs utilize plasmonic metasurfaces to control the phase and polarization of light and exploit anisotropic thin-film interference effects to enhance optical chirality while minimizing optical loss. Based on such design concepts, we demonstrated experimentally optical devices such as circular polarization filters with transmission efficiency up to 90% and extinction ratio >180, polarization converters with conversion efficiency up to 90%, as well as on-chip integrated microfilter arrays for full Stokes polarization detection with high accuracy over a broad wavelength range (3.5–5 μm). The proposed design concepts are applicable from near-infrared to Terahertz regions *via* structural engineering.

KEYWORDS: plasmonic metasurfaces, chiral metamaterials, polarization detection, polarization conversion, Stokes parameters, highly efficient, mid-infrared



INTRODUCTION

Chiral materials and molecules are useful for various applications, including optical communication,¹ CD spectroscopy,² chemical analysis,³ biomedical diagnosis,⁴ as well as polarization detection and imaging.⁵ Nevertheless, chiral materials in nature⁶ usually have weak chiral-optical effects and require long optical paths to achieve sufficiently large chirality for practical applications, resulting in fundamental limitations on device miniaturization. Recent demonstrations of chiral metamaterials^{7–20} have achieved much stronger chiral effects than their natural counterparts with ultracompact footprints. They lead to miniaturization of polarization manipulation²¹ and detection²² devices and hold the promise to enable many applications such as hologram multiplexing,^{23,24} optical encryption,²⁵ refractive index sensing,²⁶ and nonlinear imaging.²⁷

Various types of chiral metamaterial/metamaterial structures have been explored with different efficiency and performance (CD and circular polarization extinction ratio (CPE)). 3D helical metamaterials^{7,8} can achieve strong chirality (CD up to 92%, CPER \sim 18)⁷ over a broadband wavelength range with micrometer-scale thicknesses. Various types of chiral metamaterials based on planar metasurfaces have been investigated to realize ultracompact chiral optical devices with tremendous

design flexibility. The state-of-art solutions for low-loss chiral metamaterials are based on dielectric^{15–19} and dielectric–metal hybrid structures.²⁰ To date, the most efficient planar chiral metamaterial design experimentally demonstrated is based on dielectric metasurfaces¹⁵ with transmission efficiency up to 87%, yet with low CPER (<10). Alternatively, chiral metamaterials based on single or stacked planar plasmonic metasurfaces were developed with improved design flexibility and compactness.^{10–14,28,29} However, it has been very challenging to mitigate the high optical loss of plasmonic structures.^{30,31} So far, it remains challenging to achieve high-performance chiral metamaterials with both high efficiency and large CPER.

Here, we present the design concept and experimental demonstration of chiral plasmonic metamaterials (CPMs) with strong chirality (CD around 0.9, CPER > 180), high transmission efficiency (around 90%), and subwavelength

Received: March 16, 2021

Accepted: August 4, 2021

Published: August 12, 2021



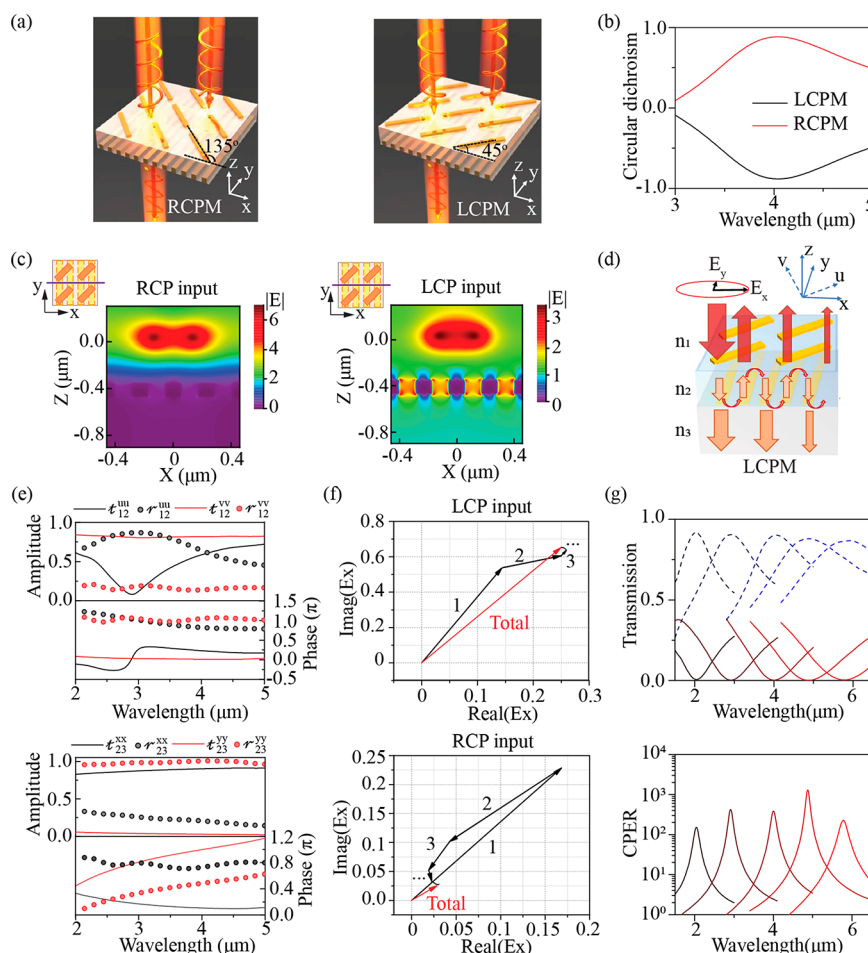


Figure 1. Design concept and simulation results of highly efficient chiral plasmonic metamaterials. (a) Schematics of the RCPM and LCPM designs. (b) Circular dichroism ($CD = T_{RCP} - T_{LCP}$) of the LCPM (red) and RCPM (black) obtained by full-wave simulation. Both structures are optimized for wavelengths around $4 \mu\text{m}$. Plasmonic nanoantennas: length 1000 nm ; width 100 nm , thickness 65 nm ; period 920 nm . Plasmonic nanograting: width 115 nm ; period 230 nm ; thickness 150 nm . The thickness of the silicon oxide spacer is 350 nm . (c) Near-field electrical field distributions (XZ plane) of the LCPM in (b) for RCP and LCP input at $4 \mu\text{m}$ obtain by full-wave simulation. (d) Schematic of the anisotropic thin-film interference model for an LCPM design. (e) Amplitude and phase of transmission (solid lines) and reflection (solid circles) coefficients of nanoantenna metasurface (top panel) and nanograting metasurface (bottom panel) in the LCPM design (b). (f) Vector plots for the complex E_x field components of transmitted light through LCPM with LCP (top panel)/RCP (bottom panel) incident light, illustrating anisotropic thin-film constructive/destructive interference effects. The orders of the transmitted partial waves are indicated with the black arrows. The total transmitted E_x field is presented with a red arrow. The E_y components are blocked by the nanogratings and hence negligible. (g) Simulated transmission spectra (top panel) and CPER (bottom panel) of LCPMs designed for different operational wavelengths from 2 to $6 \mu\text{m}$. The corresponding design parameters are provided in Table S1. Mirror images of the LCPM designs result in RCPMs for corresponding wavelengths.

thickness ($< \lambda/7$) in the mid-infrared (mid-IR) spectral range. We unveiled the reasons for such highly efficient plasmonic metamaterials with ultrastrong optical chiral effects. Based on the proposed highly efficient chiral metamaterials, we realized high-performance, efficient optical devices for polarization filtering, and conversion. By integrating the CPMs into an on-chip microscale polarization filter array, we also demonstrated full-Stokes polarization detection with high accuracy over a broad wavelength range from 3.5 to $5 \mu\text{m}$.

RESULTS AND DISCUSSION

Design Concept. The proposed CPM designs are composed of two anisotropic nonchiral plasmonic metasurfaces with a dielectric spacing layer. Figure 1a shows the schematic of two CPM designs with opposite-handedness. In both designs, the bottom metasurface consists of gold nanogratings along the y -axis. The plasmonic antennas of the top metasurfaces are

oriented at 135° (right-handed CPM) and 45° (left-handed CPM) with respect to the x -axis, resulting in chiral plasmonic structures with no inversion center or reflection symmetry. These two structures are mirror images of each other; therefore, they exhibit selective transmission for CP light with opposite-handedness, *i.e.*, right-handed CP (RCP) and left-handed CP (LCP) light. We defined the handedness of CP light from the point of view of the receiver. The circular dichroism ($CD = T_{RCP} - T_{LCP}$) of the left-handed CPM (LCPM, Figure 1a left panel) and right-handed CPM (RCPM, Figure 1a right panel) obtained *via* full-wave simulation is shown in Figure 1b. Both structures show a strong chiral response ($|CD|$ around 0.9) at wavelengths around $4 \mu\text{m}$. Simulation results of the near field distribution for the LCPM design suggest that, around the operation wavelength close to $4 \mu\text{m}$, RCP input light is mostly reflected from the nanograting layer with very low transmission $T_{RCP} < 0.3\%$ (Figure 1c, left panel) while LCP input light is transmitted

through the double-layer structure with transmission $T_{\text{LCP}} \approx 90\%$ (Figure 1c, right panel).

Unlike conventional plasmonic structures, which usually suffer from high optical loss,^{30,31} the proposed CPM structures exhibit high efficiency (up to 90%) and strong optical chiral effects with record-high CPER (>180) achieved experimentally among all the reported chiral metamaterials and metasurfaces so far. Here, we adopt an anisotropic thin-film interference model to provide an intuitive explanation of the design concept to achieve simultaneously high efficiency and high CPER of the proposed plasmonic chiral metamaterials. Figure 1d shows the schematic of the LCPM structure with the bottom gold nanograting layer oriented along the y -axis and the plasmonic antennas of the top metasurface oriented along the u -axis (45° with respect to the x -axis). For simplicity, we only consider normal incident plane wave propagating in the z -direction, which can be described as $E = E_0 e^{i(\vec{k}\vec{r} - \omega t)}$. Assuming the electric field vectors for the incident, transmitted and reflected light are $E_{\text{inc}} = \begin{pmatrix} E_{\text{inc}}^x \\ E_{\text{inc}}^y \end{pmatrix}$, $E_t = \begin{pmatrix} E_t^x \\ E_t^y \end{pmatrix}$ and $E_r = \begin{pmatrix} E_r^x \\ E_r^y \end{pmatrix}$, respectively. Multi-order transmission and reflection occur between the top and bottom metasurfaces, as illustrated in Figure 1d. Each order of transmitted and reflected electric field vectors is considered as a partial wave.³² The partial waves accumulate phase during propagation inside the spacer layer and experience abrupt phase changes upon reflection and transmission at the top and bottom metasurfaces³³ as shown in Figure 1e. The anisotropic nature of both metasurfaces results in a polarization-dependent phase and amplitude transmission/reflection; thus, it can be modeled by 2×2 matrices (see the Materials and Methods for details). The transmission and reflection coefficient for the l^{th} ($l = 1, 2, 3, \dots$) order partial waves can be described with 2×2 matrices $t^{(l)}$ and $r^{(l)}$, respectively. The total transmitted electrical field is the sum of all transmitted partial waves, $E_t = (\sum_{l=1}^{\infty} t^{(l)}) \cdot E_{\text{inc}}$ and the total reflected electric field is the sum of all reflected partial waves, $E_r = (\sum_{l=1}^{\infty} r^{(l)}) \cdot E_{\text{inc}}$. A detailed description of the theoretical model is included in the Materials and Methods. The reflection and transmission matrix elements of the top plasmonic antenna metasurface (Figure 1e) indicate its first-order resonance wavelength is around $3 \mu\text{m}$, while the operation wavelength of this CPM design is close to $4 \mu\text{m}$. Therefore, the plasmonic loss introduced by the antenna metasurfaces at the operation wavelengths is decreased to about 6%, significantly lower than that at the antenna resonance wavelength (20%, Figure S1). Moreover, to enhance the chiral optical effects and maximize the CPER at the operation wavelengths, we engineered the top and bottom plasmonic metasurfaces to achieve constructive interferences of the partial waves for LCP input light while destructive interference for RCP input light as illustrated by the phasor diagrams³² in Figure 1f. As a result, such a design is featured with very strong chirality ($\text{CD} \sim 0.9$) and a high CPER (>300 according to simulation results). In Figure 1f, the vectors' length and direction in complex planes represent the amplitude and phase of the partial waves. By adding up all the partial wave vectors, one can obtain the total transmitted field. The total transmitted field is dominated by first to third partial waves, and higher order partial waves decay exponentially. For LCP input light, the transmitted first to third partial waves exhibit similar vector directions and thus add up constructively, which leads to high transmission. In contrast, for RCP light, the transmitted second- and third-order partial waves exhibit almost opposite directions to the first order partial waves and thus add up

destructively, which leads to diminished transmission. Based on the analysis of the phasor diagrams, we conclude that device efficiency and CEPR are affected by a few factors, *i.e.*, the optical losses introduced by each metasurface, the abrupt phase changes introduced by each metasurface, and the phase accumulation and loss in the spacing layer between the two metasurfaces. The key to strong chirality and high efficiency of the CPM designs lies in rationally engineering the metasurface structures to achieve constructive/destructive interferences for CP input light with difference handedness as well as minimizing optical absorption of each plasmonic metasurfaces by shifting the device operation wavelengths away from the plasmonic resonance. The proposed structures offer great design flexibility, including geometries of the top and bottom metasurfaces, rotation angle between metasurfaces, spacer layer material and thickness, *etc.* Moreover, if necessary, one can also design structures with more than two layers of metasurfaces. Such a great design flexibility is appealing for realizing desired properties and operational wavelengths; however, it is time-consuming to perform structure optimization. Here, we employed an anisotropic transfer matrix approach to assist the design process and structure optimization (see the Materials and Methods for detailed description). Using this approach, one can employ the transmission and reflection matrices of each metasurface obtained by full-wave simulation and apply the transfer matrix model to optimize other design parameters, such as rotation angles of metasurfaces, spacing layer thickness, *etc.* Results obtained by the transfer matrix model show reasonably good agreement with the full-wave simulation results (Figure S3). More details of the transfer matrix model for anisotropic metasurfaces are provided in the Materials and Methods. Combining the transfer matrix method and full-wave simulation, we designed and optimized chiral metamaterials with high efficiency (85–92%) and high performance (CPER > 100) for the wavelength range from 2 to $6 \mu\text{m}$, as shown in Figure 1g. We notice that for longer wavelengths (> $5 \mu\text{m}$) the peak efficiency decreases due to increased optical absorption in the silicon oxide dielectric spacer layer. Other dielectric layers with low optical absorption coefficients in mid-IR wavelength can be used to improve the device efficiency for longer wavelengths.

Compared to other strategies for minimizing plasmonic loss, such as low loss plasmonic materials³⁰ and high Q plasmonic structures,³⁴ our method relies on engineering the phase and amplitude response of the plasmonic metasurfaces at off-resonance wavelengths and incorporating the anisotropic thin-film interference effects to enhanced the optical chiral effects. The plasmonic loss is greatly reduced by choosing the operation wavelengths far away from the plasmonic resonance wavelengths, while the chiral effects of the multilayer structure are enhanced by realizing constructive interference for CP input light with the desired handedness and destructive interference for the other handedness. The proposed design concepts can be expanded by incorporating various plasmonic materials to provide even greater flexibility in engineering the phase and amplitude responses for individual metasurface layers. It does not rely on realizing high Q plasmonic resonance³⁴ with narrowed resonance line width and thus is suitable for broadband applications.

Experimental Demonstration. We experimentally demonstrated subwavelength-thick highly efficient CPMs with strong chirality in the mid-IR wavelength range based on the proposed CPM designs. The devices were fabricated on sapphire substrates due to their high transmission at mid-IR wavelengths

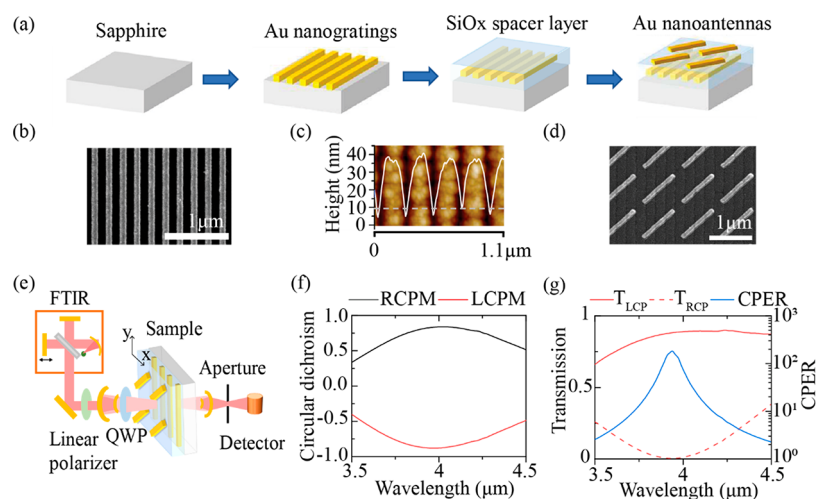


Figure 2. Device fabrication and characterization. (a) Flowchart of the device fabrication process. (b) SEM image of the nanogratings before SiOx deposition. (c) AFM image of the SiOx-covered nanogratings with height profile along the white dashed line perpendicular to nanogratings. (d) SEM image of the fabricated CPM structure. (e) Schematic of the measurement setup for CPM characterization. QWP: quarter-wave plate. (f) Measured CD for LCPM and RCPM devices. Design dimensions for LCPM/RCPM (Nanoantenna: length 1000 nm/1030 nm, thickness Cr/Au 5 nm/60 nm, period 920 nm along both x and y axes. Nanograting: width 115 nm, thickness Cr/Au 5 nm/125 nm, period 230 nm. Spacer thickness 350 nm). (g) Transmission of LCP (red solid) and RCP (red dash) input and CPER of an LCPM device with the design dimensions same as (f).

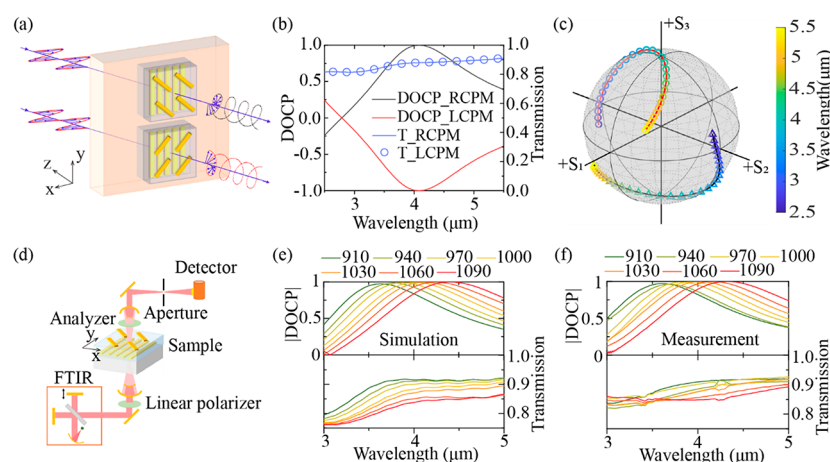


Figure 3. Polarization conversion based on CPM structures. (a) Polarization state conversion from linear polarization to elliptically polarization by the RPC (top) and LPC (bottom) devices based on RCPM and LCPM structures. Nanoantennas: length 1000 nm, width 125 nm, thickness 55 nm, period 890 nm along both the x - and y -axis. Nanogratings: width 89 nm, thickness 125 nm, period 230 nm. Spacer thickness 340 nm. (b) Simulated DOCP and transmission efficiency of LPC and RPC devices at different wavelengths. (c) Illustration of the polarization states generated by RPC (black solid) and LPC (red solid) at different wavelengths (color bar) on the Poincaré sphere. (d) Schematic of the measurement setup for polarization generation. (e) Simulated and (f) measured DOCP and transmission of the polarization converter devices for different wavelengths. Nanoantennas: length 910 nm (LPC), 940 nm (LPC), 970 nm (LPC), 1000 nm (RPC), 1030 nm (LPC), 1060 nm (LPC), 1090 nm (LPC), width 100 nm, thickness 65 nm, period 920 nm along both the x - and y -axis. Nanogratings: width 115 nm, thickness 120 nm, period 230 nm. Spacer thickness 350 nm.

up to 6 μm . Figure 2a shows the fabrication procedures. First, we patterned gold nanogratings (period: 230 nm; duty cycle: 50%; thickness: 130 nm) on top of a sapphire substrate with electron beam lithography (EBL), metal evaporation (5 nm chromium and 125 nm gold), and lift-off. Figure 2b shows a scanning electron microscope (SEM) image of the nanogratings. Then a 350 nm-thick silicon oxide spacing layer was deposited on top of the nanogratings *via* sputtering. The purpose of this spacing layer is 2-fold. First, it introduces proper propagation phase delay to achieve constructive or destructive interference for CP light with different handedness, as discussed previously in the design concept. Second, it reduces the surface height fluctuation of the regions over the 130 nm thick nanogratings. The SiOx-

covered nanograting region exhibits surface roughness $R_a = 11.4$ nm, as shown in the atomic force microscopy (AFM) image in Figure 2c. Then the gold nanoantenna metasurface was patterned on top of the spacer layer. Figure 2d shows the SEM image of a portion of the fabricated nanoantenna array. The shape and dimension of the nanoantennas were not significantly affected by the surface fluctuation. Even though the proposed chiral metamaterial designs consist of two metasurface layers, it does not require highly accurate alignment to achieve high device performance. According to our simulation results (Figure S4), a lateral displacement <200 nm between the top and bottom metasurface layers will not affect the performance of the device, and a rotation angle error between these two layers

less than 2° can maintain efficiency $>85\%$ and CPER > 200 . Besides, the device performance can preserve efficiency $>85\%$ and CPER > 100 as long as the fabrication deviations of the nanoantennas and nanogratings width and length are smaller than 20 nm and the spacer layer thickness variations are smaller than ± 20 nm (Figure S5–7). These fabrication requirements are easily satisfied with modern nanofabrication techniques.

We characterized the fabricated devices with an infrared polarization-dependent spectroscopy setup as shown in Figure 2e. Unpolarized broadband light from a Fourier transform infrared spectrometer (FTIR) was converted to circularly polarized light with a linear polarizer and a quarter-wave plate (QWP) with an operation wavelength around $4\ \mu\text{m}$ (Figure S9). The handedness of the CP light was controlled by setting the angle between the optical axis of the linear polarizer and the fast axis of the QWP to be -45° (or $+45^\circ$). We validated the generated polarization state with a polarization state analyzer (PSA) based on a rotating linear polarizer (see more details in the Materials and Methods). The light was incident onto the CPM sample, and the transmitted light was collected by a mercury cadmium telluride (MCT) detector. Figure 2f shows the measured CD spectra of an LCPM and an RCPM device, with maximum CD around 0.9 at wavelengths around $4\ \mu\text{m}$. The LCPM device exhibits transmission around 89% and CPER over 180 around $4\ \mu\text{m}$, as shown in Figure 2g. The CPER is more than 20 over a wavelength range from 3.8 to $4.1\ \mu\text{m}$. The measured CPER at wavelengths other than $4\ \mu\text{m}$ is affected by the nonideal CP input due to the limited bandwidth of the available quarter-wave plate. Considering the nonideal CP input, we analyzed the measurement results in Figure 2g to obtain the extracted transmission and CPER for the device, which show slightly improved CPER for all wavelengths (see Figure S10).

Polarization Conversion. Conventional ways for polarization conversion require bulky optics and limit system integration. Ultracompact polarization conversion devices have been demonstrated based on chiral plasmonic metamaterial and metasurface structures^{21,35,36} as well as dielectric metasurfaces.^{37–39} A dielectric metasurface based on Huygens' principle has experimentally achieved around 90% efficiency for 90° linearly polarized (LP) light rotation.⁴⁰ The CPMs we proposed can enable polarization conversion from linear to circular and elliptical polarization states with equivalent or better conversion efficiency in transmission mode compared to the state-of-art designs in the literature. Figure 3a illustrates the conversion process from LP to CP and elliptically polarized light with different handedness. LP light with electrical field vector oriented along the x -axis was incident first onto the nanograting metasurface (oriented along the y -axis) and then onto the nanoantenna metasurface. Figure 3b shows the simulated degree of circular polarization (DOCP = S_3/S_0) and transmission spectra of polarization converters based on LCPM and RCPM designs, respectively. The left-handed polarization converter (LPC) based on LCPM converts LP input light to LCP light with DOCP ~ -0.99996 at wavelengths around $4\ \mu\text{m}$. The right-handed polarization converter (RPC) based on RCPM converts LP input light to RCP light with DOCP ~ 0.99996 at wavelengths around $4\ \mu\text{m}$. The output polarization state varies with the input light wavelength. The LPC device's output polarization states exhibit DOCP ranging from -0.99996 to 0 over the wavelength range from 2.5 to $5.5\ \mu\text{m}$, with high conversion efficiencies up to 90%. In comparison, the RCP device's output polarization states exhibit DOCP from 0 to 0.99996. Due to the Helmholtz reciprocity principle, the high

efficiency of the CPM structure leads to the high conversion efficiency of the LPC and RPC. Figure 3c shows the converted polarization states on the Poincaré sphere for both devices. The generated polarization states form continuous traces on the Poincaré sphere connecting the north/south pole and the equator. The proposed polarization conversion devices can perform a similar function to the combination of a linear polarizer and a low-order QWP, yet, with subwavelength thickness ~ 520 nm ($<1/7$ of the operation wavelength).

We experimentally verified the design concepts and device functionalities with an experimental setup shown in Figure 3d. Unpolarized light from the FTIR spectrometer was first transmitted through a linear polarizer to generate LP light, then incident onto the polarization conversion device with its electrical field vector oriented perpendicular to the nanogratings and collected by the MCT detector of the FTIR system. The measurement results (Figure 3f) for LPC and RPC devices with different design parameters show reasonably good agreement with simulation results (Figure 3e). The output polarization states are wavelength dependent and can be engineered by varying the design parameters of the nanoantenna metasurfaces. The demonstrated polarization converters have high conversion efficiency up to 90% around $4\ \mu\text{m}$ and over 82% for wavelengths from 3 to $5\ \mu\text{m}$. Nearly perfect CP polarization states (IDOCPI > 0.9999) have also been generated at different wavelengths by varying the antenna lengths. One can optimize a polarization converter design to generate the desired polarization state at any wavelength of interest by changing the design parameters, such as the nanoantenna metasurface design, the spacer thickness, and the rotation angle between the two metasurfaces. Moreover, an array of devices can be integrated onto the same substrate to realize pixelated control of polarization states with spatial resolution down to a few micrometers.

Full Stokes Polarization Detection. Recently, various chiral metamaterial and metasurface structures have been demonstrated to realize ultracompact devices for polarization detection from visible (VIS) to mid-infrared (mid-IR) wavelengths.^{14,20,22,41–44} Their compactness and design flexibility are highly desirable for a wide range of applications, including biomedical diagnosis,⁴⁵ chemical analysis,⁴⁶ optical communication,⁴⁷ astronomy,⁴⁸ and target detection.⁴⁹ Yet, most of the devices are still limited by low measurement accuracy, efficiency and narrow operation wavelength range. Based on the proposed CPM structures, we demonstrated an ultracompact chip-integratable full-stokes polarization detection device with record-high measurement accuracy and broadband coverage in the mid-IR wavelength range from 3.5 to $5\ \mu\text{m}$. The device design is based on spatial division concept⁵⁰ and consists of six chip-integrated microscale polarization filters (Figure 4a, P_1 to P_6). Four linear polarization filters composed of gold nanogratings were used to selectively transmit LP light with electric field vectors oriented at angles of 90° (P_1), 0° (P_2), -45° (P_3), and 45° (P_4) with respect to the x -axis. Two circular polarization filters based on RCPM (P_5) and LCPM (P_6) selectively transmit LCP and RCP light, respectively. One empty cell (P_0) without any patterned structures is located in the center to collect total light intensity (I_0). P_5' and P_6' cells are backups for P_5 and P_6 , respectively. Note that P_5 and P_6 have nanogratings along the x -axis, while P_5' and P_6' along the y -axis. In-plane rotation of the CP filter design will not affect the performance in principle but only changes the orientation of the output electric field vector. Figure 4b shows the SEM images of the integrated polarization filter array.

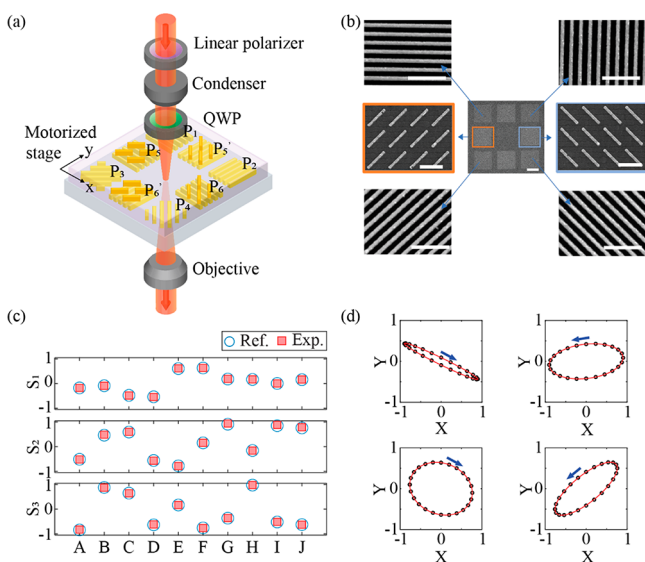


Figure 4. Full Stokes parameter detection. (a) Schematic of Stokes parameter detection setup. Unpolarized light from FTIR went through a Linear polarizer and QWP to generate an arbitrary input polarization state. Then the light went through the sample on a motorized stage, collected by an MCT detector connected with the FTIR. (b) SEMs of one polarization detection unit (in the center) with LP filters based on nanogratings oriented along four angles, *i.e.*, 0° (top left), 90° (top right), 45° (bottom left), -45° (bottom right), as well as CP filters based on RCPM (middle left) and LCPM (middle right). Scale bar: $100\ \mu\text{m}$ (detection unit) and $1\ \mu\text{m}$ (LP and CP filters). (c) Measured Stokes parameters of 10 polarization states at $4.077\ \mu\text{m}$ with our sample (red squares, exp) in comparison with the input polarization states characterized with PSA (blue circles, ref). (d) Ellipse plots for four polarization states (E, F, H, and J in (c)); black circle, measured by the PSA; red solid, measured from our device). The blue arrows indicate the handedness.

First, we adopt a widely used simple method to obtain Stokes parameters (S_0, S_1, S_2, S_3) by measuring the intensity of linear and circular polarization components (I_1 to I_6) with the polarization filter array (P_1 to P_6). For simplicity, we used relative Stokes parameters in the following discussion.

$$\begin{cases} S_0 = 1 \\ S_1 = (I_2 - I_1)/I_0 \\ S_2 = (I_4 - I_3)/I_0 \\ S_3 = (I_5 - I_6)/I_0 \end{cases} \quad (1)$$

In the experiment, we first measured each polarization filter's response to obtain the insertion loss for the corresponding polarization state it transmits (see the [Materials and Methods](#) for details). Then we generated various input polarization states by changing the rotation angle of the linear polarizer and QWP (operation wavelength around $4\ \mu\text{m}$). For each input polarization state, transmitted light through all six polarization filters was collected onto an MCT detector sequentially while moving the motorized stage. Note that it is possible to simultaneously collect light transmitted through all polarization filters at a single shot with an infrared imaging sensor, which is not available in our setup. Based on the measured light intensity, we obtained each polarization component of input light, *i.e.*, $I_0 - I_6$, taking into account the measured insertion loss of the polarization filters. Finally, we calculated the Stokes parameters of the incident light

using eq 1. To evaluate the measurement accuracy, we characterized the input polarization states with a PSA (see the [Materials and Methods](#)). Figure 4c shows the comparison between the measured Stokes parameters obtained by our device and reference values obtained by the PSA for ten different polarization states. Figure 4d shows the ellipse plots for four polarization states (E, F, H, and G mentioned in Figure 4c). The average measurement errors for $S_1, S_2,$ and S_3 are 0.0044, 0.014, and 0.0079, respectively, and the measurement errors for DOCP and DOLP are 0.0079 and 0.015, respectively. To the best of our knowledge, we have achieved the highest measurement accuracy among all metasurface/metamaterial-based full-Stokes polarization detection devices reported in the literature so far, as summarized in a previous paper.²⁰ The measurement accuracy is limited by the linear polarization extinction ratio (LPER) of the linear polarization filters and CPER of the circular polarization filters. Therefore, despite the simplicity and trivial computation requirements, this method can only provide high measurement accuracy for a limited wavelength range ($\sim 100\ \text{nm}$), over which the circular polarization filters exhibit high CPER (>100). To achieve a high-accuracy polarization measurement over a broad wavelength range, we also developed another method based on the Muller matrix for polarization detection over the whole wavelength range from 3.5 to $5\ \mu\text{m}$.

Figure 5a illustrates the Muller matrix based method with a flowchart. Before measuring arbitrary input polarization states, the Muller matrix elements on the first row for each polarization filter were determined with a set of calibrated polarization states as input, as described in the [Materials and Methods](#). Figure 5b shows the extracted Muller matrix elements on the first row for P_1, P_5 and P_6 filters over the wavelength range from 3.5 to $5\ \mu\text{m}$. Figure S11 shows the measured Muller matrix elements of other polarization filters. To characterize an unknown polarization state ($\vec{S}_{\text{in}} = (S_0, S_1, S_2, S_3)$) for each wavelength λ , we measured the transmitted light intensity through each filter in sequence using the FTIR and a microscope with a motorized stage. The relation between the output intensity through the six polarization filters ($I^{P_1}(\lambda), I^{P_2}(\lambda), I^{P_3}(\lambda), I^{P_4}(\lambda), I^{P_5}(\lambda), I^{P_6}(\lambda)$) and the input polarization state $\vec{S}_{\text{in}}(\lambda)$ can be described by the following equation.

$$\begin{pmatrix} I^{P_1}(\lambda) \\ I^{P_2}(\lambda) \\ I^{P_3}(\lambda) \\ I^{P_4}(\lambda) \\ I^{P_5}(\lambda) \\ I^{P_6}(\lambda) \end{pmatrix} = A_{6 \times 4}(\lambda) \cdot I_0(\lambda) \begin{pmatrix} S_0(\lambda) \\ S_1(\lambda) \\ S_2(\lambda) \\ S_3(\lambda) \end{pmatrix} \quad (2)$$

where $I_0(\lambda)$ is the input light intensity obtained by the empty cell P_0 , and the matrix $A_{6 \times 4}(\lambda)$ consists of the Muller matrix elements of all six polarization filters obtained previously:

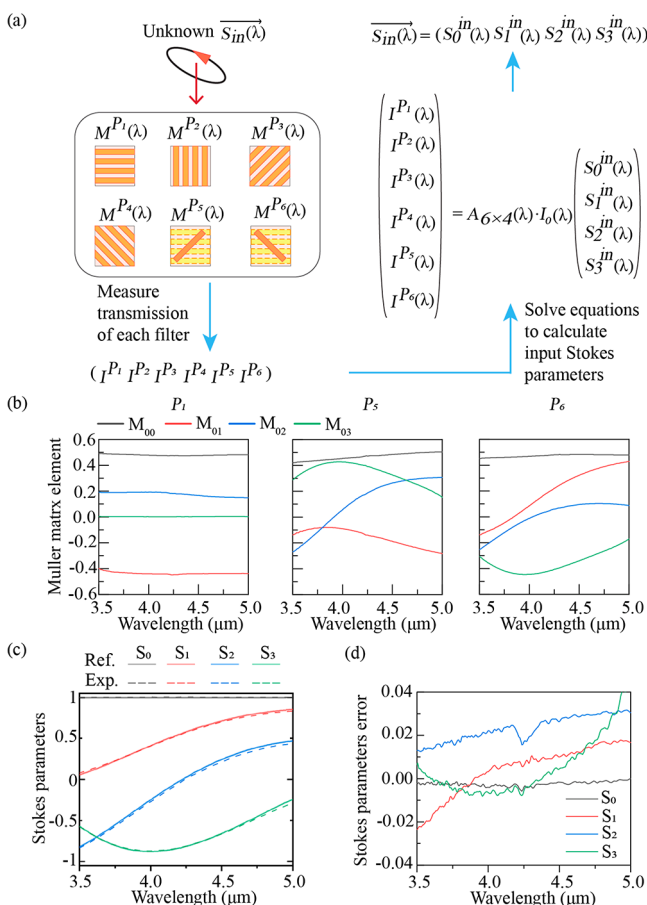


Figure 5. Broadband full-Stokes polarization detection. (a) Flowchart for broadband polarization detection process based on the Muller matrix method. The transmission of normal incident light with unknown polarization states through each polarization filter is measured with FTIR. Then based on Muller Matrix calculation, we can calculate the input polarization states. (b) Muller matrix elements (on the first row) of polarization filter P_1 (left), P_3 (middle), and P_6 (right). (c) Broadband Stokes parameter measurement results obtained by the PSA (solid line, ref) and our device (dashed line, exp) for different polarization states from 3.5 to 5 μm . (d) Measurement errors for Stokes parameters as functions of wavelength (corresponding to measurement results presented in (c)).

$$A_{6 \times 4}(\lambda) = \begin{pmatrix} M_{00}^{P_1} & M_{01}^{P_1} & M_{02}^{P_1} & M_{03}^{P_1} \\ M_{00}^{P_2} & M_{01}^{P_2} & M_{02}^{P_2} & M_{03}^{P_2} \\ M_{00}^{P_3} & M_{01}^{P_3} & M_{02}^{P_3} & M_{03}^{P_3} \\ M_{00}^{P_4} & M_{01}^{P_4} & M_{02}^{P_4} & M_{03}^{P_4} \\ M_{00}^{P_5} & M_{01}^{P_5} & M_{02}^{P_5} & M_{03}^{P_5} \\ M_{00}^{P_6} & M_{01}^{P_6} & M_{02}^{P_6} & M_{03}^{P_6} \end{pmatrix} \quad (3)$$

During the experiment, we generated different input polarization states from 3.5 to 5 μm with a linear polarizer and a low-order QWP. Since the retardance of the QWP is dispersive, the generated beam will have different Stokes parameters ($S_0(\lambda)$, $S_1(\lambda)$, $S_2(\lambda)$, $S_3(\lambda)$) at different wavelengths. We measured the transmitted light intensity through all six polarization filters to obtain the vector on the left of eq 2. According to the Rouché–

Capelli theorem, the existence of a unique solution for eq 2 requires the rank of the matrix $A_{6 \times 4}(\lambda)$ to be 4. This requirement can be satisfied as long as the LPERs of P_1 , P_2 , P_3 , and P_4 and CPERs of P_5 , P_6 are not equal to 1 at the wavelengths of interest. In practice, since the noise is unavoidable during measurement, large LPERs and CPERs are desirable to achieve high measurement accuracy. Figure 5c shows the measured Stokes parameters with our devices from 3.5 to 5 μm , which agrees well with the reference values obtained by the PSA. The corresponding measurement errors of all Stokes parameters at different wavelengths are shown in Figure 5d. The proposed measurement method achieved small measurement errors over the entire 3.5 to 5 μm wavelength range. The measurement errors can be further reduced by increasing the polarization filters' extinction ratios and improving measurement accuracy for the polarization filters' Muller matrix elements.

So far, we have shown that the Muller matrix method allows highly accurate measurement of polarization state over a broad wavelength range with a set of rigorous calculation procedures. In contrast, for single wavelength measurement, the first method is much simpler and faster. Both methods can be used for single-shot full-Stokes polarization detection by integrating these polarization filter arrays directly with photodetector arrays or imaging sensors; thus, they are promising for ultracompact polarization detectors or imaging sensors with high speed, high accuracy, and broadband wavelength coverage.

CONCLUSION

We have demonstrated design strategies for realizing high-performance chiral plasmonic metamaterials based on anisotropic thin-film interferences effects facilitated by metasurface structures. Strong chirality was achieved in subwavelength-thick all-plasmonic metamaterials with minimized optical loss, which has been one of the major limitations for various plasmonic devices.^{30,31} The resulted CPM structures are featured with high efficiency (up to 90%), large CD (around 0.9) and CPER (up to 180), and subwavelength thickness ($<\lambda/7$). Compared with other chiral metamaterial designs reported in literature, our device achieved simultaneously high optical efficiency, strong CD and largest CPER, as shown in Figure 6. We have applied the demonstrated CPMs to a few device applications, such as circular polarization filters, polarization conversion, and full-Stokes polarization detection. The circular polarization filters exhibit simultaneously high CPER (up to 180) and transmission efficiency (around 90%). The polarization converters showed high polarization conversion efficiency (up to 90%) from LP to CP and elliptically polarized light and produced near-perfect CP light with IDOCP up to 0.99998. By integrating the circular polarization filters with nanograting-based linear polarization filters on the same chip, we demonstrated full-Stokes polarization detection with record-high measurement accuracy and broadband wavelength coverage from 3.5 to 5 μm . The proposed CPM design concepts are readily applicable for other wavelengths from near IR to THz. They hold great promise to enable ultracompact, high-performance devices for various applications, such as optical communication, biomedical diagnosis, polarization imaging, and spectroscopy.

MATERIALS AND METHODS

Numerical Simulations. The full-wave simulations were performed using Lumerical FDTD (Lumerical, Inc.). The material optical properties are obtained from the Lumerical library. We simulated the unit cell with the normal incidence of plane wave source(s) propagating

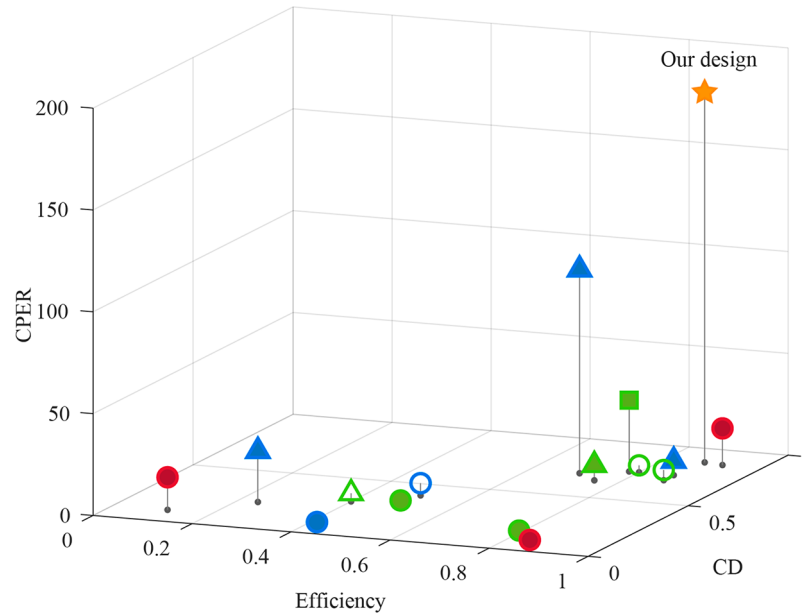


Figure 6. Comparison of efficiency, CD, and CPER with other chiral metamaterial designs based on 3D helical structures^{7,8} plasmonic,^{9–14} and dielectric^{15–19} and hybrid²⁰ metamaterial/metasurfaces. Each design's operation wavelength is indicated with color (visible, blue; near IR, green; mid-IR, red). The material of each design is indicated with shape (triangle, dielectric; circle, plasmonic; square, hybrid). Solid/hollow shapes represent structures operated in transmission/reflection mode. The performance of the proposed CPM design is represented by a star.

in negative z -direction, periodic in-plane boundary conditions, and perfectly matched layer (PML) out-of-plane boundary conditions. For CPM simulation, two orthogonally placed LP sources with $\pm \pi/2$ relative phase retardance go through the nanoantenna metasurface, dielectric spacing layer, gold nanograting, and sapphire substrate. For oblique incidence cases, we used Bloch boundary conditions, combined the results from two individual orthogonal-placed LP sources, and made sure the incident angle was the same over the full wavelength range in the simulation.

Thin-Film Interference Model for Anisotropic Metasurfaces.

Each metasurface introduces different abrupt phase and amplitude changes for transmitted and reflected light.³³ Due to the top and bottom metasurfaces' anisotropic light responses, the reflection and transmission coefficients for normal incidence on each metasurface are modeled by 2×2 matrices⁵¹

$$r_{mn} = \begin{pmatrix} r_{mn}^{xx} & r_{mn}^{yx} \\ r_{mn}^{xy} & r_{mn}^{yy} \end{pmatrix} \quad (4)$$

$$t_{mn} = \begin{pmatrix} t_{mn}^{xx} & t_{mn}^{yx} \\ t_{mn}^{xy} & t_{mn}^{yy} \end{pmatrix} \quad (5)$$

where $r_{mn}^{xy} = \frac{E_n^y}{E_m^x}$ ($m, n = 1, 2, 3$) represents the complex amplitude of the reflected electric field incident from medium m to n propagating along the negative z -direction, linearly polarized in the y -direction for excitation in the x -direction, similarly for t_{mn}^{xy} . We obtained the reflection and transmission coefficients of the metasurfaces from full-wave simulation results (FDTD). We first exported the amplitude and phase of the reflected and transmitted electric fields along the X - and Y -directions for X -polarized or Y -polarized LP input light normally incident on the nanogratings, respectively. The nanograting is oriented along the y -axis. Similarly, we can obtain the reflected and transmitted electric fields of nanoantenna metasurface. The nanoantennas are oriented along the u -axis. Since the incident light field amplitude is 1, the reflection and transmission coefficients are the same as the obtained complex electric field.

The reflection and transmission coefficients of nanoantenna metasurface along UV coordinates as defined in Figure 1d were transformed to XY coordinates by applying rotation matrix

$\text{ROT}(\theta) = \begin{pmatrix} \cos(\theta) & -\sin(\theta) \\ \sin(\theta) & \cos(\theta) \end{pmatrix}$ in the following equations (see Figure S2 for transmission and reflection coefficients of nanoantenna metasurface in XY coordinates)

$$r'_{mn}(\theta) = \text{ROT}(-\theta) \cdot r_{mn} \cdot \text{ROT}(\theta) \quad (6)$$

$$t'_{mn}(\theta) = \text{ROT}(-\theta) \cdot t_{mn} \cdot \text{ROT}(\theta) \quad (7)$$

where θ is the rotation angle between UV and XY coordinates.

Since the x -axis we chose is perpendicular or parallel to the nanograting, the off-diagonal terms of r_{12} , t_{12} , r_{21} , and t_{21} are all zero. For the nanoantenna metasurface, after transferring the UV coordinates to XY coordinates, the off-diagonal terms of r_{23} , t_{23} , r_{32} , and t_{32} are non-zero, indicating the interconversion between the x and y field components (E_x and E_y) upon light incidence onto the anisotropic metasurfaces.

The l th order of reflection coefficient for our device with light normally incident from the air onto nanoantenna array, followed by the SiOx spacer and nanogratings, can be calculated as

$$r^{(l)} = \begin{cases} r_{12}, & l = 1 \\ t_{21} \cdot r_{23} \cdot (r_{21} \cdot r_{23})^{l-2} \cdot t_{12} \cdot e^{i2(l-1)k_2 d}, & l \geq 2 \end{cases} \quad (8)$$

where $k_2 = \frac{2\pi}{\lambda} n_2$ and d is the spacer thickness. The total reflected field can be expressed as $(\sum_{l=1}^{\infty} r^{(l)}) \cdot E_{\text{inc}}$, and the total reflectivity is

$$R_{\text{tot}} = \frac{|\sum_{l=1}^{\infty} r^{(l)} \cdot E_{\text{inc}}|^2}{|E_{\text{inc}}|^2}$$

Similarly, the l th order of the transmitted electric field can be calculated as

$$t^{(l)} = t_{23} \cdot (r_{21} \cdot r_{32})^{l-1} \cdot t_{12} \cdot e^{i(2l-1)k_2 d} \quad (9)$$

The total transmitted field can be expressed as $(\sum_{l=1}^{\infty} t^{(l)}) \cdot E_{\text{inc}}$, and the

$$\text{total transmission is } T_{\text{tot}} = \frac{|\sum_{l=1}^{\infty} t^{(l)} \cdot E_{\text{inc}}|^2}{|E_{\text{inc}}|^2} \cdot \frac{\text{Re}(n_3)}{\text{Re}(n_1)}$$

Transfer-Matrix Model for Anisotropic Metasurfaces. We adopted a transfer-matrix approach (4×4 matrix) to model the relation between the complex reflection coefficients r_{mn}^{xy} , transmission

coefficients t_{mn}^{xy} , and the forward and backward propagating electric field through our device⁵²

$$\begin{pmatrix} E_{3b} \\ E_{3f} \end{pmatrix} = \begin{pmatrix} M_1 & M_2 \\ M_3 & M_4 \end{pmatrix} \begin{pmatrix} E_{1b} \\ E_{1f} \end{pmatrix} \quad (10)$$

where M_1 , M_2 , M_3 , and M_4 are each 2×2 matrix relating the electric fields before the top nanoantenna metasurface and after the bottom nanogratings.

$$\begin{pmatrix} M_1 & M_2 \\ M_3 & M_4 \end{pmatrix} = \begin{pmatrix} t_{32}^{-1} & t_{32}^{-1} r_{23} \\ r_{32} t_{32}^{-1} & r_{32} t_{32}^{-1} r_{23} + t_{23} \end{pmatrix} \begin{pmatrix} e^{-ik_2 d} I & Z \\ Z & e^{ik_2 d} I \end{pmatrix} \begin{pmatrix} t_{21}^{-1} & t_{21}^{-1} r_{12} \\ r_{21} t_{21}^{-1} & r_{21} t_{21}^{-1} r_{12} + t_{12} \end{pmatrix} \quad (11)$$

Here, r_{mn} and t_{mn} are the reflectance and transmittance matrix, $I = \begin{pmatrix} 0 & 1 \\ 1 & 0 \end{pmatrix}$, $Z = \begin{pmatrix} 0 & 0 \\ 0 & 0 \end{pmatrix}$, $k_2 = \frac{2\pi}{\lambda} n_2$, and d is the spacer thickness. The complex reflection and transmission coefficients at each interface at various wavelengths used in the transfer matrix are obtained directly from FDTD simulation. Since there is no backward electric field in the

substrate, i.e., $E_{3b} = \begin{pmatrix} 0 \\ 0 \end{pmatrix}$, for a given incident field, $E_{1f} = \begin{pmatrix} E_x e^{i\phi_x} \\ E_y e^{i\phi_y} \end{pmatrix}$, the

reflected and transmitted electric fields from our device, E_{1b} and E_{3f} , can be calculated with the transfer matrix. The transmission spectra obtained from FDTD simulation, thin-film interference model and transfer matrix approach (Figure S3) agree reasonably well. The difference between the transmission spectra is resulting from the assumption that R_{mn} and T_{mn} obtained from FDTD simulation have a plane wave incident at each interface. For a very thin SiOx spacer layer, the interlayer interaction between the nanoantenna metasurface and nanogratings is strong. The electric field incident from the nanoantenna to the nanograting is not precisely a plane wave. Nevertheless, this is a good approximation for simplifying the calculation.

Fabrication. Fabrication Procedures. Gold Nanograting. Thin layer of Cr (~6 nm) was thermally evaporated onto a sapphire substrate as the discharging layer. Double-layer PMMA (200 nm 495 K + 70 nm 950 K) was then spin-coated on the Cr layer. Then nanograting patterns were written with EBL (JEOL JBX-6000FS). The samples were then developed in MIBK: IPA (1:3) solution for 2 min and rinse with DI water. After that, the PMMA residue was removed with O₂ plasma (Plasma-Therm 790, O₂ 10 sccm, 8 mT, 25W) for 18s. Next, Cr (5 nm)/Au (125 nm) was deposited with thermal evaporation, lifted-off in acetone, and rinsed with IPA. The Cr discharging layer was then removed by Cr dry etching (PlasmaLab M80 Plus, Cl₂/O₂ 38/2 sccm, 40s).

SiOx Spacer Layer. The sample was cleaned by O₂ plasma (Plasma-Therm 790, O₂ 10 sccm, 8 mT, 25W) for 3 min and deposited with 349 nm SiOx by Sputtering (Lesker PVD 75, 0.5 Å/s).

Gold Nanoantennas. The sample was coated with a thin layer of Cr (~6 nm) by thermal evaporation and spin-coated with double layer PMMA (100 nm 495 K + 70 nm 950 K). The sample is then patterned with EBL, developed in MIBK/IPA, and cleaned with O₂ plasma as described earlier. After that, Cr (5 nm) \ Au (60 nm) was thermally evaporated on the sample and lifted off in acetone. The Cr discharging layer was then removed by Cr dry etching (PlasmaLab M80 Plus, Cl₂/O₂ 38/2 sccm, 40s).

EBL Alignment. We first fabricated four cross-shaped alignment markers and the bottom nanograting layer on the same sample at the same time by EBL. Then we performed EBL alignment with the markers on the bottom layer during the top layer fabrication to compensate for the relative rotations and offset of the sample in the EBL cassette. After that, we can pattern the nanoantennas in the desired directions or angles relative to the bottom layer with rotation accuracy better than 1°.

Film Thickness Control. We first calibrated the deposition rate and optical properties of sputtered silicon oxide thin films on Si wafers with an Atomic Force Microscope (AFM, Bruker MultiMode 8) and an

ellipsometer (Woollam M2000). For device fabrication, we put a monitor sample (silicon wafer) beside the device during the silicon oxide deposition. In this way, we could control the silicon oxide layer thickness with less than 10 nm deviation.

Measurement. We performed optical characterization of devices with a Bruker Vertex 70 FTIR spectrometer and Hyperion 2000 microscope. We used one 15× objective and one condenser lenses with N.A. = 0.4 in the experiment.

Device Efficiency Characterization. Unpolarized light from FTIR was first polarized to the desired polarization state with a linear polarizer (LPMIR100) and a QWP (Thorlabs, WPLQ05M-4000). For example, CP was generated for CPM device characterization and LP light for LPC device characterization. Then we collected transmitted light through the metasurface device (intensity: I_{device}) and an empty region on the same substrate ($I_{\text{substrate}}$) with the mid-IR microscope coupled with the FTIR. We calculated the transmission of the device using the formula $T_{\text{device}} = \frac{I_{\text{device}}}{I_{\text{substrate}}} (1 - R_T)$, where R_T is the measured reflection from the top surface of substrate (silicon oxide layer on top of sapphire).

Broadband Polarization States Measurement with a PSA Based on a Rotating Linear Polarizer. The conventional way to measure polarization state utilizes a QWP (Thorlabs, WPLQ05M-4000) and a linear polarizer. However, it was not feasible for the polarization measurement over the entire 3–5 μm in our experiment because of the limited bandwidth of the mid-IR QWP and limited space in the FTIR microscope setup. Therefore, we used a different method with only one linear polarizer to perform polarization state measurement, which can be used for purely polarized light.

The Jones vector can describe any polarized input light as $J = \begin{pmatrix} E_{x0} \\ E_{y0} e^{i\delta} \end{pmatrix}$, where E_{x0} and E_{y0} are the amplitudes of electric field

components along the x - and y -axis and δ ($-180^\circ < \delta \leq 180^\circ$) is the phase difference between the electric field components in the x - and y -directions, respectively. After light passes through a rotating linear polarizer, the angle-dependent transmission can be described with the following equation

$$T(\alpha) = |E_{x0} \cos \alpha + E_{y0} e^{i\delta} \sin \alpha|^2 \quad (12)$$

where α is the angle between the optical axis of the linear polarizer and the x -axis.

Or alternatively

$$T(\alpha) = E_{x0}^2 \cos^2 \alpha + E_{y0}^2 \sin^2 \alpha + E_{x0} E_{y0} \sin 2\alpha \cos \delta \quad (13)$$

With measurements at three values for angle α , we obtained E_{x0} , E_{y0} , and $|\delta|$ and then calculated the corresponding Stokes parameters. The sign for phase difference δ was determined based on the preknowledge of the setup or device. For polarization states generated by the linear polarizer and quarter waveplate, the sign of the δ was determined by the retardance of the QWP obtained from the datasheet. For polarization states generated by the CPM-based polarization converters, the sign of the δ was determined based on the FDTD simulation results. Additional measurements at more angles can help to increase the measurement accuracy with the least-mean-square method. We carried out at least 13 measurements for different rotation angles (α) to characterize each input polarization state (Figure S8). The measurement accuracy is sensitive to the linear polarization extinction ratio (LPER) of the polarizer. The polarizers (Thorlabs, LPMIR100) we used have LPER higher than 4×10^4 , introducing less than 0.7% error in the Stokes parameter measurement.

Full Stokes Parameter Detection Based on CPM Structures. To obtain each polarization filter's transmission coefficient, we generated six polarization states, including LP light polarized along 90, 0, -45, and 45°, LCP light, and RCP light, and measured the transmission through the microscale polarization filters, $P_1 - P_6$, correspondingly.

For Stokes parameter detection measurement, we generated arbitrary polarization states of the input light by rotating the linear polarizer and quarter waveplate (QWP, operation wavelength around 4 μm). To determine the measurement accuracy, we characterized the input polarization states with the PSA as described previously in the

Materials and Methods. Then the sign of S_3 was estimated based on the retardance curve of the QWP from the vendor. After that, we replaced the PSA with our sample, refocused, and measured the transmission of each of the six polarization filters by moving the motorized stage and selecting the points of interest with an aperture at the image plane.

Muller Matrix Characterization of the Device. The polarization response of an optical device or system can be described by a Muller matrix M , which links the input polarization states $\vec{S}_{in} = (S_0, S_1, S_2, S_3)$ and the output polarization states $\vec{S}_{out} = (S'_0, S'_1, S'_2, S'_3)$ written in the form of Stokes parameters.

$$\begin{pmatrix} S'_0 \\ S'_1 \\ S'_2 \\ S'_3 \end{pmatrix} = \begin{pmatrix} M_{00} & M_{10} & M_{20} & M_{30} \\ M_{01} & M_{11} & M_{21} & M_{31} \\ M_{02} & M_{12} & M_{22} & M_{32} \\ M_{03} & M_{13} & M_{23} & M_{33} \end{pmatrix} \begin{pmatrix} S_0 \\ S_1 \\ S_2 \\ S_3 \end{pmatrix} \quad (14)$$

From eq 14, the output light intensity (S'_0) can be obtained with the first row of the Muller matrix and \vec{S}_{in}

$$S'_0 = M_{00}S_0 + M_{10}S_1 + M_{20}S_2 + M_{30}S_3 \quad (15)$$

We determined the Muller matrix's first row for each polarization filter by transmitting four polarization states with known Stokes parameters measured with the PSA and measuring the corresponding output Stokes parameters for each of the filters. Then we can solve the following equation to obtain the Muller matrix elements ($M_{00}(\lambda)$ $M_{10}(\lambda)$ $M_{20}(\lambda)$ $M_{30}(\lambda)$) at each wavelength

$$\begin{pmatrix} S_0^{Pol'_1} \\ S_0^{Pol'_2} \\ S_0^{Pol'_3} \\ S_0^{Pol'_4} \end{pmatrix} = \begin{pmatrix} S_0^{Pol_1} & S_0^{Pol_2} & S_0^{Pol_3} & S_0^{Pol_4} \\ S_1^{Pol_1} & S_1^{Pol_2} & S_1^{Pol_3} & S_1^{Pol_4} \\ S_2^{Pol_1} & S_2^{Pol_2} & S_2^{Pol_3} & S_2^{Pol_4} \\ S_3^{Pol_1} & S_3^{Pol_2} & S_3^{Pol_3} & S_3^{Pol_4} \end{pmatrix} \begin{pmatrix} M_{00} \\ M_{10} \\ M_{20} \\ M_{30} \end{pmatrix} \quad (16)$$

where S_i^{pol} is the Stokes parameter S_i ($i = 0-3$) for polarization state number j and $S_0^{pol'}$ is the measured output intensity through the polarization filter for polarization state number j .

The determinant of the matrix in eq 16 should be non-zero to have a unique solution for the Muller matrix elements. More than four polarization states can be used to solve the overconstrained equation to obtain the Muller Matrix with the least-mean-square method for higher accuracy. Here, we measured six input polarization states and obtained the Muller matrix elements for all six polarization filters.

ASSOCIATED CONTENT

Supporting Information

The Supporting Information is available free of charge at <https://pubs.acs.org/doi/10.1021/acsnano.1c02278>.

Simulation for optical loss introduced by the nanoantenna and nanograting; the amplitude of transmission and reflection coefficients of rotated nanoantenna; design parameters of LCPM for wavelength engineering; comparison between different simulation methods; detailed discussion about the tolerance fabrication imperfection; reference polarization states measurement with PSA; Stokes parameters measurement for CP light generated for CPM characterization; calibration for nonideal input polarization states; Muller matrix elements of other polarization filters (PDF)

AUTHOR INFORMATION

Corresponding Author

Yu Yao – School of Electrical, Computer and Energy Engineering and Center for Photonic Innovation, Arizona State University, Tempe, Arizona 85287, United States; orcid.org/0000-0003-4892-052X; Phone: (480) 965-9208; Email: yuyao@asu.edu

Author

Jing Bai – School of Electrical, Computer and Energy Engineering and Center for Photonic Innovation, Arizona State University, Tempe, Arizona 85287, United States; orcid.org/0000-0003-3867-7925

Complete contact information is available at: <https://pubs.acs.org/10.1021/acsnano.1c02278>

Author Contributions

Y.Y. and J.B. conceived the idea. J.B. performed the theoretical analysis, device fabrication, and characterization. Both authors analyzed the results and contributed to the manuscript.

Notes

The authors declare no competing financial interest.

ACKNOWLEDGMENTS

This work was supported in part by AFOSR YIP under Grant No. FA9550-16-1-0183, NSF under Grant No. 1809997, and DOE under Grant No. DE-EE0008999. Device fabrication and characterization in the Center for Solid State Electronics Research (CSSER) and LeRoy Eyring Center for Solid State Science (LE-CSSS) at Arizona State University was supported, in part, by NSF contract ECCS-1542160. The authors acknowledge a helpful discussion on theoretical modeling and coding with Dr. Ali Basiri and suggestions on device fabrication from Dr. Chao Wang and Dr. Xiahui Chen.

REFERENCES

- (1) Farshchi, R.; Ramsteiner, M.; Herfort, J.; Tahraoui, A.; Grahm, H. T. Optical Communication of Spin Information between Light Emitting Diodes. *Appl. Phys. Lett.* **2011**, *98* (16), 162508.
- (2) Kelly, S. M.; Jess, T. J.; Price, N. C. How to Study Proteins by Circular Dichroism. *Biochim. Biophys. Acta, Proteins Proteomics* **2005**, *1751* (2), 119–139.
- (3) Baykusheva, D.; Zindel, D.; Svoboda, V.; Bommeli, E.; Ochsner, M.; Tehlar, A.; Wörner, H. J. Real-Time Probing of Chirality during a Chemical Reaction. *Proc. Natl. Acad. Sci. U. S. A.* **2019**, *116* (48), 23923.
- (4) Tuchin, V. V.; Wang, L. V.; Zimnyakov, D. A. *Optical Polarization in Biomedical Applications*; Springer: Berlin, 2006; p ix, 281 p.
- (5) Hegedüs, R.; Szél, G.; Horváth, G. Imaging Polarimetry of the Circularly Polarizing Cuticle of Scarab Beetles (Coleoptera: Rutelidae, Cetoniidae). *Vision Res.* **2006**, *46* (17), 2786–2797.
- (6) Mun, J.; Kim, M.; Yang, Y.; Badloe, T.; Ni, J.; Chen, Y.; Qiu, C.-W.; Rho, J. Electromagnetic Chirality: From Fundamentals to Nontraditional Chiroptical Phenomena. *Light: Sci. Appl.* **2020**, *9*, 139.
- (7) Gansel, J. K.; Thiel, M.; Rill, M. S.; Decker, M.; Bade, K.; Saile, V.; von Freymann, G.; Linden, S.; Wegener, M. Gold Helix Photonic Metamaterial as Broadband Circular Polarizer. *Science* **2009**, *325* (5947), 1513–1515.
- (8) Frank, B.; Yin, X.; Schäferling, M.; Zhao, J.; Hein, S. M.; Braun, P. V.; Giessen, H. Large-Area 3D Chiral Plasmonic Structures. *ACS Nano* **2013**, *7* (7), 6321–6329.
- (9) Zhang, M.; Pacheco-Peña, V.; Yu, Y.; Chen, W.; Greybush, N. J.; Stein, A.; Engheta, N.; Murray, C. B.; Kagan, C. R. Nanoimprinted Chiral Plasmonic Substrates with Three-Dimensional Nanostructures. *Nano Lett.* **2018**, *18* (11), 7389–7394.

- (10) Li, W.; Coppens, Z. J.; Besteiro, L. V.; Wang, W.; Govorov, A. O.; Valentine, J. Circularly Polarized Light Detection with Hot Electrons in Chiral Plasmonic Metamaterials. *Nat. Commun.* **2015**, *6*, 8379.
- (11) Tang, B.; Li, Z.; Palacios, E.; Liu, Z.; Butun, S.; Aydin, K. Chiral-Selective Plasmonic Metasurface Absorbers Operating at Visible Frequencies. *IEEE Photonics Technol. Lett.* **2017**, *29* (3), 295–298.
- (12) Ouyang, L.; Wang, W.; Rosenmann, D.; Czaplowski, D. A.; Gao, J.; Yang, X. Near-Infrared Chiral Plasmonic Metasurface Absorbers. *Opt. Express* **2018**, *26* (24), 31484–31489.
- (13) Zhao, Y.; Belkin, M. A.; Alù, A. Twisted Optical Metamaterials for Planarized Ultrathin Broadband Circular Polarizers. *Nat. Commun.* **2012**, *3* (1), 870.
- (14) Bai, J.; Wang, C.; Chen, X.; Basiri, A.; Wang, C.; Yao, Y. Chip-Integrated Plasmonic Flat Optics for Mid-Infrared Full-Stokes Polarization Detection. *Photonics Res.* **2019**, *7* (9), 1051–1060.
- (15) Zhu, A. Y.; Chen, W. T.; Zaidi, A.; Huang, Y.-W.; Khorasaninejad, M.; Sanjeev, V.; Qiu, C.-W.; Capasso, F. Giant Intrinsic Chiro-Optical Activity in Planar Dielectric Nanostructures. *Light: Sci. Appl.* **2018**, *7*, 17158.
- (16) Hu, J.; Zhao, X.; Lin, Y.; Zhu, A.; Zhu, X.; Guo, P.; Cao, B.; Wang, C. All-Dielectric Metasurface Circular Dichroism Waveplate. *Sci. Rep.* **2017**, *7*, 41893.
- (17) Semnani, B.; Flannery, J.; Al Maruf, R.; Bajcsy, M. Spin-Preserving Chiral Photonic Crystal Mirror. *Light: Sci. Appl.* **2020**, *9* (1), 23.
- (18) Groever, B.; Rubin, N. A.; Mueller, J. P. B.; Devlin, R. C.; Capasso, F. High-Efficiency Chiral Meta-Lens. *Sci. Rep.* **2018**, *8* (1), 7240.
- (19) Khorasaninejad, M.; Chen, W. T.; Zhu, A. Y.; Oh, J.; Devlin, R. C.; Rousso, D.; Capasso, F. Multispectral Chiral Imaging with a Metalens. *Nano Lett.* **2016**, *16* (7), 4595–4600.
- (20) Basiri, A.; Chen, X.; Bai, J.; Amrollahi, P.; Carpenter, J.; Holman, Z.; Wang, C.; Yao, Y. Nature-Inspired Chiral Metasurfaces for Circular Polarization Detection and Full-Stokes Polarimetric Measurements. *Light: Sci. Appl.* **2019**, *8* (1), 78.
- (21) Qin, F.; Ding, L.; Zhang, L.; Monticone, F.; Chum, C. C.; Deng, J.; Mei, S.; Li, Y.; Teng, J.; Hong, M.; Zhang, S.; Alù, A.; Qiu, C.-W. Hybrid Bilayer Plasmonic Metasurface Efficiently Manipulates Visible Light. *Science Advances* **2016**, *2* (1), e1501168.
- (22) Afshinmanesh, F.; White, J. S.; Cai, W.; Brongersma, M. L. Measurement of the Polarization State of Light Using an Integrated Plasmonic Polarimeter. *Nanophotonics* **2012**, *1* (2), 125.
- (23) Wen, D.; Yue, F.; Li, G.; Zheng, G.; Chan, K.; Chen, S.; Chen, M.; Li, K. F.; Wong, P. W. H.; Cheah, K. W.; Yue Bun Pun, E.; Zhang, S.; Chen, X. Helicity Multiplexed Broadband Metasurface Holograms. *Nat. Commun.* **2015**, *6* (1), 8241.
- (24) Hu, Y.; Li, L.; Wang, Y.; Meng, M.; Jin, L.; Luo, X.; Chen, Y.; Li, X.; Xiao, S.; Wang, H.; Luo, Y.; Qiu, C.-W.; Duan, H. Trichromatic and Tripolarization-Channel Holography with Noninterleaved Dielectric Metasurface. *Nano Lett.* **2020**, *20* (2), 994–1002.
- (25) Luo, X.; Hu, Y.; Li, X.; Jiang, Y.; Wang, Y.; Dai, P.; Liu, Q.; Shu, Z.; Duan, H. Integrated Metasurfaces with Microprints and Helicity-Multiplexed Holograms for Real-Time Optical Encryption. *Adv. Opt. Mater.* **2020**, *8* (8), 1902020.
- (26) Wu, Z.; Chen, X.; Wang, M.; Dong, J.; Zheng, Y. High-Performance Ultrathin Active Chiral Metamaterials. *ACS Nano* **2018**, *12* (5), 5030–5041.
- (27) Rodrigues, S. P.; Lan, S.; Kang, L.; Cui, Y.; Cai, W. Nonlinear Imaging and Spectroscopy of Chiral Metamaterials. *Adv. Mater.* **2014**, *26* (35), 6157–6162.
- (28) Chen, W.; Abeyinghe, D. C.; Nelson, R. L.; Zhan, Q. Experimental Confirmation of Miniature Spiral Plasmonic Lens as a Circular Polarization Analyzer. *Nano Lett.* **2010**, *10* (6), 2075–2079.
- (29) Wang, J. J.; Walters, F.; Liu, X.; Sciortino, P.; Deng, X. High-Performance, Large Area, Deep Ultraviolet to Infrared Polarizers Based on 40 Nm Line/78 Nm Space Nanowire Grids. *Appl. Phys. Lett.* **2007**, *90* (6), 061104.
- (30) Boriskina, S. V.; Cooper, T. A.; Zeng, L.; Ni, G.; Tong, J. K.; Tsurimaki, Y.; Huang, Y.; Meroueh, L.; Mahan, G.; Chen, G. Losses in Plasmonics: From Mitigating Energy Dissipation to Embracing Loss-Enabled Functionalities. *Adv. Opt. Photonics* **2017**, *9* (4), 775–827.
- (31) Khurgin, J. B. How to Deal with the Loss in Plasmonics and Metamaterials. *Nat. Nanotechnol.* **2015**, *10* (1), 2–6.
- (32) Kats, M. A.; Blanchard, R.; Ramanathan, S.; Capasso, F. Thin-Film Interference in Lossy, Ultra-Thin Layers. *Opt. Photonics News* **2014**, *25* (1), 40–47.
- (33) Yu, N.; Capasso, F. Flat Optics with Designer Metasurfaces. *Nat. Mater.* **2014**, *13*, 139.
- (34) Wang, B.; Yu, P.; Wang, W.; Zhang, X.; Kuo, H.-C.; Xu, H.; Wang, Z. M. *Adv. Opt. Mater.* **2021**, *9* (7), 2001520.
- (35) Wu, P. C.; Tsai, W.-Y.; Chen, W. T.; Huang, Y.-W.; Chen, T.-Y.; Chen, J.-W.; Liao, C. Y.; Chu, C. H.; Sun, G.; Tsai, D. P. Versatile Polarization Generation with an Aluminum Plasmonic Metasurface. *Nano Lett.* **2017**, *17* (1), 445–452.
- (36) Yu, N.; Aieta, F.; Genevet, P.; Kats, M. A.; Gaburro, Z.; Capasso, F. A Broadband, Background-Free Quarter-Wave Plate Based on Plasmonic Metasurfaces. *Nano Lett.* **2012**, *12* (12), 6328–6333.
- (37) Rubin, N. A.; Zaidi, A.; Juhl, M.; Li, R. P.; Mueller, J. P. B.; Devlin, R. C.; Leósson, K.; Capasso, F. Polarization State Generation and Measurement with a Single Metasurface. *Opt. Express* **2018**, *26* (17), 21455–21478.
- (38) Yang, Y.; Wang, W.; Moitra, P.; Kravchenko, I. I.; Briggs, D. P.; Valentine, J. Dielectric Meta-Reflectarray for Broadband Linear Polarization Conversion and Optical Vortex Generation. *Nano Lett.* **2014**, *14* (3), 1394–1399.
- (39) Arbabi, A.; Horie, Y.; Bagheri, M.; Faraon, A. Dielectric Metasurfaces for Complete Control of Phase and Polarization with Subwavelength Spatial Resolution and High Transmission. *Nat. Nanotechnol.* **2015**, *10*, 937.
- (40) Kruk, S.; Hopkins, B.; Kravchenko, I. I.; Miroshnichenko, A.; Neshev, D. N.; Kivshar, Y. S. *Invited Article: Broadband Highly Efficient Dielectric Metadevices for Polarization Control* **2016**, *1* (3), 030801.
- (41) Chen, W. T.; Torok, P.; Foreman, M. R.; Liao, C. Y.; Tsai, W. Y.; Wu, P. R.; Tsai, D. P. Integrated Plasmonic Metasurfaces for Spectropolarimetry. *Nanotechnology* **2016**, *27* (22), 224002.
- (42) Arbabi, E.; Kamali, S. M.; Arbabi, A.; Faraon, A. Full-Stokes Imaging Polarimetry Using Dielectric Metasurfaces. *ACS Photonics* **2018**, *5* (8), 3132–3140.
- (43) Rubin, N. A.; D'Aversa, G.; Chevalier, P.; Shi, Z.; Chen, W. T.; Capasso, F. Matrix Fourier Optics Enables a Compact Full-Stokes Polarization Camera. *Science* **2019**, *365* (6448), eaax1839.
- (44) Yang, Z.; Wang, Z.; Wang, Y.; Feng, X.; Zhao, M.; Wan, Z.; Zhu, L.; Liu, J.; Huang, Y.; Xia, J.; Wegener, M. Generalized Hartmann-Shack Array of Dielectric Metalens Sub-Arrays for Polarimetric Beam Profiling. *Nat. Commun.* **2018**, *9* (1), 4607.
- (45) Kunnen, B.; Macdonald, C.; Doronin, A.; Jacques, S.; Eccles, M.; Meglinski, I. Application of Circularly Polarized Light for Non-Invasive Diagnosis of Cancerous Tissues and Turbid Tissue-Like Scattering Media. *Journal of Biophotonics* **2015**, *8* (4), 317–323.
- (46) Nafie, L. A. Vibrational Circular Dichroism: A New Tool for the Solution-State Determination of the Structure and Absolute Configuration of Chiral Natural Product Molecules. *Natural Product Communications*. March 2008.
- (47) Roberts, K.; Sullivan, M. O.; Wu, K.; Sun, H.; Awadalla, A.; Krause, D. J.; Laperle, C. Performance of Dual-Polarization Qpsk for Optical Transport Systems. *J. Lightwave Technol.* **2009**, *27* (16), 3546–3559.
- (48) Ichimoto, K.; Lites, B.; Elmore, D.; Suematsu, Y.; Tsuneta, S.; Katsukawa, Y.; Shimizu, T.; Shine, R.; Tarbell, T.; Title, A.; Kiyohara, J.; Shinoda, K.; Card, G.; Lecinski, A.; Streander, K.; Nakagiri, M.; Miyashita, M.; Noguchi, M.; Hoffmann, C.; Cruz, T. Polarization Calibration of the Solar Optical Telescope Onboard Hinode. In *The Hinode Mission*, Sakurai, T., Ed.; Springer: New York, 2008; pp 179–207.
- (49) Tyo, J. S.; Goldstein, D. L.; Chenault, D. B.; Shaw, J. A. Review of Passive Imaging Polarimetry for Remote Sensing Applications. *Appl. Opt.* **2006**, *45* (22), 5453–5469.

(50) Gruev, V.; Perkins, R.; York, T. Ccd Polarization Imaging Sensor with Aluminum Nanowire Optical Filters. *Opt. Express* **2010**, *18* (18), 19087–19094.

(51) Yeh, P. Electromagnetic Propagation in Birefringent Layered Media. *J. Opt. Soc. Am.* **1979**, *69* (5), 742–756.

(52) Pfeiffer, C.; Grbic, A. Bianisotropic Metasurfaces for Optimal Polarization Control: Analysis and Synthesis. *Phys. Rev. Appl.* **2014**, *2*, 044011 DOI: [10.1103/PhysRevApplied.2.044012](https://doi.org/10.1103/PhysRevApplied.2.044012).